1868 *Inorg. Chem.* **2011**, *50*, 1868–1878
DOI: 10.1021/ic102304m

Inorganic Chemistry
Article

Carbon Monoxide Dehydrogenase Reaction Mechanism: A Likely Case of Abnormal CO_2 Insertion to a Ni−H^- Bond

Patricia Amara,*,† Jean-Marie Mouesca,‡ Anne Volbeda,† and Juan C. Fontecilla-Camps*,†

†*Laboratoire de Cristallographie et de Cristallogenèse des Protéines, Institut de Biologie Structurale J.P. Ebel CEA, CNRS, Université Joseph Fourier 41, rue Jules Horowitz, 38027 Grenoble, France, and*
‡*Laboratoire de Chimie Inorganique et Biologique UMR-E 3 CEA-UJF, CEA-INAC 17 avenue des Martyrs, 38054 Grenoble, France*

Received November 18, 2010

Ni-containing carbon monoxide dehydrogenases (CODH), present in many anaerobic microorganisms, catalyze the reversible oxidation of CO to CO_2 at the so-called C-cluster. This atypical active site is composed of a $[NiFe_3S_4]$ cluster and a single unusual iron ion called ferrous component II or Fe_u that is bridged to the cluster via one sulfide ion. After additional refinement of recently published high-resolution structures of $COOH_x$-, OH_x-, and CN-bound CODH from *Carboxydothermus hydrogenoformans* (Jeoung and Dobbek *Science* **2007**, *318*, 1461−1464; *J. Am. Chem. Soc.* **2009**, *131*, 9922−9923), we have used computational methods on the predominant resulting structures to investigate the spectroscopically well-characterized catalytic intermediates, C_{red1} and the two-electron more-reduced C_{red2}. Several models were geometry-optimized for both states using hybrid quantum mechanical/molecular mechanical potentials. The comparison of calculated Mössbauer parameters of these active site models with experimental data allows us to propose that the C_{red1} state has a Fe_u−Ni^{2+} bridging hydroxide ligand and the C_{red2} state has a hydride terminally bound to Ni^{2+}. Using our combined structural and theoretical data, we put forward a revised version of an earlier proposal for the catalytic cycle of Ni-containing CODH (Volbeda and Fontecilla-Camps *Dalton Trans.* **2005**, *21*, 3443−3450) that agrees with available spectroscopic and structural data. This mechanism involves an abnormal CO_2 insertion into the Ni^{2+}−H^- bond.

Introduction

Anaerobic bacteria such as *Carboxydothermus hydrogenoformans* (*Ch*) and *Rhodospirillum rubrum* (*Rr*) can use CO as a source of carbon and low-potential electrons thanks to the presence of Ni-containing carbon monoxide dehydrogenases (CODH)[1] that catalyzes the reversible reaction $CO + H_2O \leftrightarrow CO_2 + 2e^- + 2H^+$. In the acetogenic bacterium *Moorella thermoacetica* (*Mt*), CODH forms a complex with another enzyme of the Wood−Ljungdahl pathway of carbon fixation,[2] acetyl-coenzyme A synthase (ACS): CO_2 is reduced to CO, which diffuses through a 70-Å-long tunnel[1] before reaching the ACS active site where it combines with CoA and a methyl group to synthesize acetyl-CoA. CODH and ACS are also found in acetyl-CoA decarbonylase/synthase complexes of methanogenic archaea.[3] After metal and acid-labile sulfide content analyses revealed that CODH was a nickel-containing, iron−sulfur protein,[4] numerous spectroscopic studies followed.[5−15] The reversible CO oxidation by CODH was found to occur at the so-called C-cluster[16] assumed to be composed of Ni and a $[Fe_4S_4]^{+1}$ cluster with spin $S = 1/2$ in

*To whom correspondence should be addressed. E-mail: patricia.amara@ibs.fr (P.A.); juan.fontecilla@ibs.fr (J.C.F.-C.).

(1) Fontecilla-Camps, J. C.; Amara, P.; Cavazza, C.; Nicolet, Y.; Volbeda, A. *Nature* **2009**, *460*(7257), 814–822.
(2) Ragsdale, S. W.; Pierce, E. *Biochim. Biophys. Acta, Proteins Proteomics* **2008**, *1784*(12), 1873–1898.
(3) Grahame, D. A. *Trends Biochem. Sci.* **2003**, *28*(5), 221–224.
(4) Ragsdale, S. W.; Clark, J. E.; Ljungdahl, L. G.; Lundie, L. L.; Drake, H. L. *J. Biol. Chem.* **1983**, *258*(4), 2364–2369.
(5) Lindahl, P. A.; Münck, E.; Ragsdale, S. W. *J. Biol. Chem.* **1990**, *265*(7), 3873–3879.
(6) Lindahl, P. A.; Ragsdale, S. W.; Münck, E. *J. Biol. Chem.* **1990**, *265*(7), 3880–3888.
(7) Anderson, M. E.; Lindahl, P. A. *Biochemistry* **1994**, *33*(29), 8702–8711.
(8) Anderson, M. E.; Lindahl, P. A. *Biochemistry* **1996**, *35*(25), 8371–8380.
(9) Hu, Z. G.; Spangler, N. J.; Anderson, M. E.; Xia, J. Q.; Ludden, P. W.; Lindahl, P. A.; Münck, E. *J. Am. Chem. Soc.* **1996**, *118*(4), 830–845.
(10) Seravalli, J.; Kumar, M.; Lu, W. P.; Ragsdale, S. W. *Biochemistry* **1997**, *36*(37), 11241–11251.
(11) DeRose, V. J.; Telser, J.; Anderson, M. E.; Lindahl, P. A.; Hoffman, B. M. *J. Am. Chem. Soc.* **1998**, *120*(34), 8767–8776.
(12) Spangler, N. J.; Meyers, M. R.; Gierke, K. L.; Kerby, R. L.; Roberts, G. P.; Ludden, P. W. *J. Biol. Chem.* **1998**, *273*(7), 4059–4064.
(13) Ralston, C. Y.; Wang, H. X.; Ragsdale, S. W.; Kumar, M.; Spangler, N. J.; Ludden, P. W.; Gu, W.; Jones, R. M.; Patil, D. S.; Cramer, S. P. *J. Am. Chem. Soc.* **2000**, *122*(43), 10553–10560.
(14) Chen, J. Y.; Huang, S.; Seravalli, J.; Gutzman, H.; Swartz, D. J.; Ragsdale, S. W.; Bagley, K. A. *Biochemistry* **2003**, *42*(50), 14822–14830.
(15) Gu, W. W.; Seravalli, J.; Ragsdale, S. W.; Cramer, S. P. *Biochemistry* **2004**, *43*(28), 9029–9035.

 Published on Web 01/19/2011

its reduced states identified by EPR.[5,6,12] The $g_{av} = 1.82$ EPR signal (later assigned to the state called C_{red1}[8]) was altered by CN^-, which acts as a strong inhibitor of CO oxidation. ENDOR data suggested that CN^- binds the C-cluster directly, most probably at the CO binding site.[16] The state giving rise to the $g_{av} = 1.86$ EPR signal (later called C_{red2}[8]) is thought to be two-electron more-reduced than C_{red1}. Although both ligands bind to C_{red1}, neither CN^- nor CO bind to C_{red2}, indicating that CO is oxidized by the enzyme in the C_{red1} state.[7,8,10] One of the proposed putative $[Fe_4S_4]$ cluster Fe ions was assigned to the so-called ferrous component II (FCII) identified in a Mössbauer study.[6] Later, the C_{red1} state was described as containing also a ferrous component III (FCIII), in addition to two iron ions belonging to a $Fe^{II}Fe^{III}$ mixed-valence pair.[9] Although it was difficult to identify the Mössbauer signals from the C_{red2} state, given the presence of Fe ions in other clusters, the authors concluded that its spectrum should be very similar to the one from C_{red1}. A later ENDOR study of the C_{red1} state suggested that an observed strongly coupled solvent-exchangeable proton signal originates from a hydroxide bound to FCII.[11] This signal was lost in the C_{red2} state or after CN^- treatment. In addition, a nitrogen ENDOR signal was attributed to a histidine ligand of the putative $[Fe_4S_4]^{+1}$ cluster, whereas no ^{61}Ni ENDOR signal was observed in either C_{red1} or C_{red2}. Finally, Ni L-edge and K-edge X-ray absorption spectroscopic studies favored a low-spin diamagnetic Ni^{2+} for both states, although high-spin Ni^{2+} was also observed.[13,15]

Some interpretations from the spectroscopic studies described above[17] were challenged and others confirmed when CODH crystal structures became available. In 2001, the 1.63 Å resolution X-ray model of *Ch*CODH revealed a dimer with three standard $[Fe_4S_4]$ clusters corresponding to two B-clusters and a novel D-cluster bound at the subunits' interface,[18] involved in electron transfer. X-ray crystallographic anomalous dispersion experiments showed that in the C-cluster Ni is actually part of the cubane adding to a distorted $[Fe_3S_4]$ moiety, while a single iron atom corresponding to FCII (also called the unique iron, Fe_u) is linked to the $[NiFe_3S_4]$ cluster via a sulfide ion. The *Ch*CODH model included a μ_2-sulfido ligand between the Ni and Fe_u atoms.[19] Given that (1) this bridging sulfide was not found in subsequent structures of *Rr*CODH,[20] *Mt*CODH,[21,22] or recombinant *Ch*CODH[23] and (2) sulfide reversibly inhibited *Rr*CODH and *Mt*CODH,[24] it may be concluded that the observed μ_2-S is not a component of the active species. Drennan and co-workers[20] proposed a binding mode for COOH at the C-cluster of the *Rr*CODH X-ray structure where the carbon atom interacts with both Ni and Fe_u and its oxygen atoms interact with a histidine and a lysine, respectively. In 2005, some of us,[25] on the basis of previous spectroscopic and crystallographic data on CODH*s* and the observation that COS is also a substrate,[26] proposed a mechanism for reversible CO oxidation in which, instead of the sulfide ion discussed above, the C_{red1} state has a $Ni-Fe_u$ bridging OH^- (similar to the Ni−B state in [NiFe]-hydrogenase[27]). Furthermore, the redox-active species[11] in the two-electron more-reduced C_{red2} state was proposed to be a hydride.[25]

In 2007, Jeoung and Dobbek reported high resolution crystal structures of *Ch*CODH with catalytically relevant ligands bound at the C-cluster active site.[23] Two structures with an OH_x-bound C-cluster from samples poised at −320 mV and −600 mV were interpreted as corresponding to the C_{red1} and C_{red2} states, respectively (models **I** and **IV** in Figure 1). Another sample poised at −600 mV and treated with bicarbonate led to a structure with a $COOH_x$-bound C-cluster (model **III** in Figure 1). Following this work, the X-ray structure of *Methanosarcina barkeri* (*Mb*) CODH[28] suggested simultaneous binding of a putative CO ligand to Ni and OH_x to Fe_u, a species that would correspond to intermediate **II** in Figure 1.

Taking advantage of Jeoung and Dobbek's high resolution C-cluster structures,[23] we decided to employ hybrid quantum mechanical (QM)/molecular mechanical (MM) techniques[29−31] to investigate the intermediate states in the reversible CO oxidation at the C-cluster, including the effect of the protein environment. However, we found that the published structures contained unexplained electron density. Consequently, we further refined the crystallographic structures of *Ch*CODH,[23] introducing, when necessary, partially occupied structural components in order to obtain essentially flat residual $[F_{obs} - F_{calc}]$ electron density maps. This procedure led to better refinement statistics, at the same time revealing several features relevant to catalysis. We also noticed that although Jeoung and Dobbek[23] have assigned the nonbridging Fe_u-bound OH_x-containing structures poised at −320 mV and −600 mV to the C_{red1} and C_{red2} states, respectively, they are almost identical. Consequently, we compared calculated Mössbauer parameters from these models with experimental data in order to check the validity of the published hypotheses concerning these reduced states.[23,25,32] During this study, reports on the structural bases for CN^- inhibition of *Ch*CODH[33] and *Mt*CODH[34] were also published. Consequently, we have also characterized the CN^- inhibited state of the former. Taken together, our results allow for the proposal of a mechanism that involves a $Ni-H^-$ species in

(16) Anderson, M. E.; Derose, V. J.; Hoffman, B. M.; Lindahl, P. A. *J. Am. Chem. Soc.* **1993**, *115*(25), 12204–12205.
(17) Lindahl, P. A. *Biochemistry* **2002**, *41*(7), 2097–2105.
(18) Dobbek, H.; Svetlitchnyi, V.; Gremer, L.; Huber, R.; Meyer, O. *Science* **2001**, *293*(5533), 1281–1285.
(19) Dobbek, H.; Svetlitchnyi, V.; Liss, J.; Meyer, O. *J. Am. Chem. Soc.* **2004**, *126*(17), 5382–5387.
(20) Drennan, C. L.; Heo, J. Y.; Sintchak, M. D.; Schreiter, E.; Ludden, P. W. *Proc. Natl. Acad. Sci. U.S.A.* **2001**, *98*(21), 11973–11978.
(21) Doukov, T. I.; Iverson, T. M.; Seravalli, J.; Ragsdale, S. W.; Drennan, C. L. *Science* **2002**, *298*(5593), 567–572.
(22) Darnault, C.; Volbeda, A.; Kim, E. J.; Legrand, P.; Vernede, X.; Lindahl, P. A.; Fontecilla-Camps, J. C. *Nat. Struct. Biol.* **2003**, *10*(4), 271–279.
(23) Jeoung, J. H.; Dobbek, H. *Science* **2007**, *318*(5855), 1461–1464.
(24) Feng, J.; Lindahl, P. A. *J. Am. Chem. Soc.* **2004**, *126*(29), 9094–9100.
(25) Volbeda, A.; Fontecilla-Camps, J. C. *Dalton Trans.* **2005**, *21*, 3443–3450.
(26) Ensign, S. A. *Biochemistry* **1995**, *34*(16), 5372–5381.
(27) Volbeda, A.; Martin, L.; Cavazza, C.; Matho, M.; Faber, B. W.; Roseboom, W.; Albracht, S. P. J.; Garcin, E.; Rousset, M.; Fontecilla-Camps, J. C. *J. Biol. Inorg. Chem.* **2005**, *10*(3), 239–249.
(28) Gong, W.; Hao, B.; Wei, Z.; Ferguson, D. J.; Tallant, T.; Krzycki, J. A.; Chan, M. K. *Proc. Natl. Acad. Sci. U. S. A.* **2008**, *105*(28), 9558–9563.
(29) Friesner, R. A.; Guallar, V. *Annu. Rev. Phys. Chem.* **2005**, *56*, 389–427.
(30) Lin, H.; Truhlar, D. G. *Theor. Chem. Acc.* **2007**, *117*(2), 185–199.
(31) Senn, H. M.; Thiel, W. QM/MM methods for biological systems. In *Atomistic Approaches in Modern Biology: from Quantum Chemistry to Molecular Simulations*; Springer-Verlag: Berlin, 2007; Vol. *268*, pp 173−290.
(32) Lindahl, P. A. *Angew. Chem., Int. Ed.* **2008**, *47*(22), 4054–4056.
(33) Jeoung, J. H.; Dobbek, H. *J. Am. Chem. Soc.* **2009**, *131*(29), 9922–9923.
(34) Kung, Y.; Doukov, T. I.; Seravalli, J.; Ragsdale, S. W.; Drennan, C. L. *Biochemistry* **2009**, *48*(31), 7432–7440.

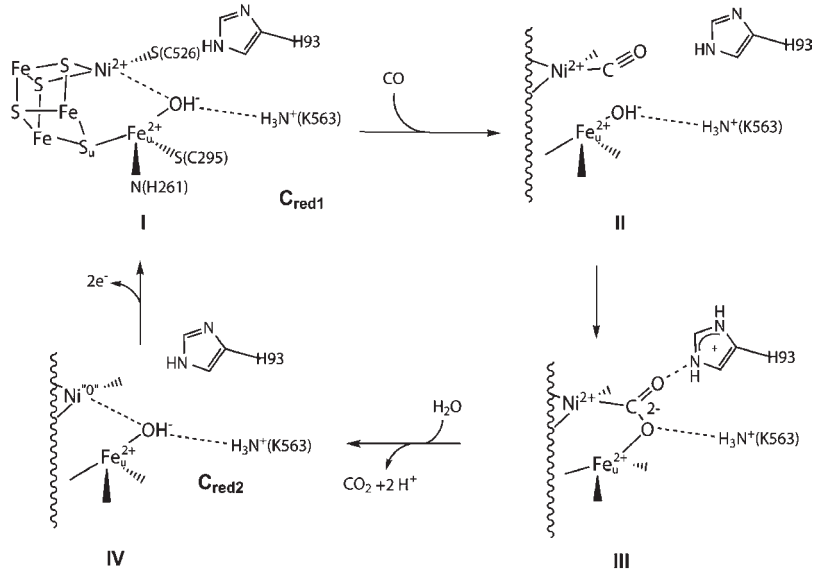

Figure 1. C-cluster reaction mechanism. Although the C-cluster reaction mechanism is reversible, the scheme proposed by Jeoung and Dobbek[23] is only depicted in the CO oxidation direction for simplicity.

the C_{red2} state resulting in the "abnormal" CO_2 insertion, which leads to a metallocarboxylate[35] rather than the standard metal-bound formate generated by "normal" CO_2 insertion.[36,37]

Materials and Methods

Structure Refinements. Using the Coot program,[38] we noticed that many features in the residual electron density maps were left unexplained when using the high resolution published atomic models [OH-600], [COO-600], [OH-320], and [CN-320] (X-ray model names indicate the ligand and the reported imposed redox potential). These structures correspond to PDB codes 3B51, 3B52, 3B53,[23] and 3I39,[33] respectively. Accordingly, we decided to resume their refinements using the PDB-deposited structure factors. Taking advantage of the high observation-to-parameter ratio, we applied individual anisotropic temperature factors with the program Refmac[39] to all non-hydrogen atoms and not only to metal cluster atoms, as Jeoung and Dobbek did. Overall, the quality of the electronic density maps was improved, and better refinement statistics were obtained (Table S1, Supporting Information). The most significant modifications in the active site region were the addition of (1) a second conformation for an eight-residue segment (260−267) and nearby residues 365 and 366 in all models, (2) an up to 35% occupied COO in both [OH-320] and [OH-600], and (3) a 35% occupied CO and water molecule in [COO-600] (see below). Other modifications are described in detail in the Supporting Information. All of the revised X-ray models are designated as above with an added *rev* tag.

Figures 3−6 and S1 and S2 were prepared with the MOLSCRIPT[40] and RASTER3D[41] programs, and the electron density map was displayed using the CONSCRIPT[42] program. The cavity map in Figure 3 was calculated with the CAVsel program, based on CAVEnv.[43]

Enzyme Hybrid Quantum Mechanical (QM)/Molecular Mechanical (MM) Modeling. All modeling and simulations of enzyme models were performed using programs in the Schrödinger suite.[44] With the exception of the CN^--bound and the corresponding H^--bound starting models (see below), we used the major conformation of the $COOH_x$-bound CODH X-ray model in our calculations. Hydrogens were built and minimized, and protonation states of titrable residues and water orientations were optimized. The quantum part consists of (1) the $[NiFe_3S_4]$ cluster and the unique iron Fe_u; (2) Cys333, Cys426, and Cys476, which coordinate the Fe atoms of the cluster; 3) His261 and Cys295, which are ligands of Fe_u; (4) Cys526, which is a Ni ligand; (5) all of the tested nonprotein ligands COO^{2-}, $COOH^-$, O^{2-}, OH^-, H^-, and H_2O, used to discriminate between various models as explained below; and (6) Lys563 and His93, which interact with these ligands, and Asp219, which interacts with His93. Geometry was optimized with the QSite program;[44] the LACVP** basis set[45,46] was used for metals, whereas the 6-31G** basis set was used for all other atoms treated quantum mechanically. Density functional theory (DFT) with the B3LYP functional was used for the QM part, while the OPLS-2005 force field[47] was employed for the rest of the enzyme. Link atoms[48] ensured the junction between the QM (Cβ atom) and the MM (Cα atom) parts of cysteines 295, 333, 426, 476, and 526; histidines 93 and 261; Lys563; and Asp219. His93 (Figure 1) was either singly protonated on Nδ (proton interacting with the carboxylate group of Asp219) or doubly protonated with Nε, interacting with nonprotein ligands at the active site. The presence or absence of an additional water (called W_e) found in the [OH-320], [OH-320*rev*], and [COO-600*rev*] structures was also tested along with Ni oxidation states +2 and 0.

(35) Vol'pin, M. E.; Kolomnikov, I. S. *Pure Appl. Chem.* **1973**, *33*, 567–582.
(36) Jessop, P. G.; Ikariya, T.; Noyori, R. *Chem. Rev.* **1995**, *95*(2), 259–272.
(37) Darensbourg, D. J. *Inorg. Chem.* **2010**, *49* (23), 10765−10780.
(38) Emsley, P.; Lohkamp, B.; Scott, W. G.; Cowtan, K. *Acta Crystallogr.* **2010**, *D66*, 486–501.
(39) Murshudov, G. N.; Vagin, A. A.; Dodson, E. J. *Acta Crystallogr.* **1997**, *D53*, 240–255.
(40) Kraulis, P. J. *J. Appl. Crystallogr.* **1991**, *24*, 946–950.
(41) Merritt, E. A.; Bacon, D. J. *Methods Enzymol.* **1997**, *277*, 505–524.
(42) Lawrence, M. C.; Bourke, P. *J. Appl. Crystallogr.* **2000**, *33*, 990–991.
(43) Collaborative Computational Project Number 4. *Acta Crystallogr.* **1994**, *D50*, 760–763.
(44) (a) *Maestro, v.b.Q.*, version 5.5; (c) Jaguar, version 7.5; Schrödinger, LLC: New York, 2009.
(45) Hay, P. J.; Wadt, W. R. *J. Chem. Phys.* **1985**, *82*(1), 299–310.
(46) Dunietz, B. D.; Beachy, M. D.; Cao, Y.; Whittington, D. A.; Lippard, S. J.; Friesner, R. A. *J. Am. Chem. Soc.* **2000**, *122*, 2828–2839.
(47) Jorgensen, W. L.; Maxwell, D. S.; Tirado-Rives, J. *J. Am. Chem. Soc.* **1996**, *118*(45), 11225–11236.
(48) Amara, P.; Field, M. J. *Theor. Chem. Acc.* **2003**, *109*(1), 43–52.

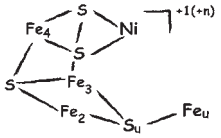

Figure 2. Atom name assignments in the C-cluster ($n = 0$ or $+2$).

Given the significant number of models, we decided to adopt a notation that may appear cumbersome but has the advantage of being explicit: [Ligand,$His^{(+)}$,(W_e)]Ni^n, where (1) the non-protein ligand is indicated without its charge, (2) the protonation state of His93 is denoted by its total charge, (3) the presence of the *extra* water is indicated by W_e and its absence by --, and (4) the oxidation state of Ni is specified by *n*. All of the constructed models are defined in the Supporting Information. The starting position of the oxygen atom of ligands O^{2-}, OH^-, H_2O, and of H^- corresponds to the one occupied by the oxygen ligand in the [OH-320] and [OH-600] X-ray models. Because there is a significant conformational change of the 260−267 amino acid segment and nearby residues 365 and 366 between the main conformations of [COO-600] and [CN-320], we used the major conformation of these residues in the latter as a starting structure for the CN^--bound CODH. The [†CN,His^+,--]Ni^{2+} model was built, where the † sign indicates (1) the major alternative conformation of the 260−267 amino acid segment found in [CN-320] (called †Seg) compared to its counterpart in [COO-600] (called Seg) and (2) the alternative position of the unique iron (called $^{\dagger}Fe_u$) compared to its counterpart in [COO-600] (called Fe_u). For this model, His93 was doubly protonated because of the short 2.69 Å distance between the N atom of CN^- and the Nε of His93 in the crystal structure. We also built the corresponding H^--bound form, the [†H,His^+,--]Ni^{2+} model, and two models with Ni^0, no ligand, and either Seg or †Seg.

Here, we have assumed that the available X-ray models are structurally representative of the electronic structures found by EPR and Mössbauer spectroscopy. EPR studies have shown that the [$Fe_uFe_3S_4$] moiety exhibits a signal similar to a standard $[Fe_4S_4]^{+1}$ $S = 1/2$ cluster.[12,17] It consists of a mixed-valence ($Fe^{2.5+}$−$Fe^{2.5+}$) pair of spin $S = 9/2$ and a ferrous (Fe^{2+}−Fe^{2+}) pair of spin $S = 4$, antiferromagnetically coupled. We approach this pure spin $S = 1/2$ state by building corresponding broken symmetry (BS) states (see ref 49 for details). These states of mixed spin ($Ms = 1/2$) and spatial broken symmetry exhibit local high-spin iron ions ($S = 5/2$ or 2 for ferric or ferrous ions, respectively). We geometry-optimized the QM/MM [COO, His,--]Ni^{2+} model for the six possible BS states. These optimized structures are very similar; the energies of the models where Fe_2−Fe_4, Fe_3−Fe_4, and Fe_u−Fe_4 are the mixed-valence pairs are within 20 kJ mol^{-1}, whereas models where Fe_u−Fe_2, Fe_u−Fe_3, and Fe_2−Fe_3 are the mixed-valence pairs are higher in energy (∼40 to 60 kJ mol^{-1}). We retained Fe_u−Fe_4 as the (localized) mixed-valence pair and Fe_2−Fe_3 as the ferrous pair (Figure 2) in our working model for further geometry optimizations because it corresponds to the lowest energy for [COO, His,--]Ni^{2+}.

Note: Subsequent Mössbauer data calculations on quantum models showed that the pair combination where (Fe_3−Fe_4) is the mixed-valence pair is the only one that fits the experimental data. Therefore, we also tested the QM/MM optimization of our COO^-- and H^--containing models with this combination, but no significant changes in the geometry were observed.

Ni L-edge X-ray spectroscopy suggested that the Ni atom is mostly low spin ($S = 0$) Ni^{2+},[13] which is consistent with its square planar coordination in the $COOH_x$-bound crystal structure,[23] but a fraction of high spin ($S = 1$) Ni^{2+} was also observed.[13] We have confirmed that the $S = 0$ is more stable by about 58 kJ mol^{-1}. Consequently, the Ni^{2+} spin was set to 0 in our calculations on all models with coplanar Ni coordination (two inorganic sulfur atoms from the [Fe_3S_4] moiety; the Cys526 thiolate; and either C of COO^-, C of CN^-, H^-, or nothing).

The geometries of all constructed models were optimized on the QM/MM potential surface. First, the MM part was optimized with a decreasing harmonic constraint from 6.0 to 1.2 kJ $Å^{-2}$ mol^{-1} holding the QM part fixed, and then, the whole QM/MM system was allowed to move.

QM Model Systems of Relevant States for Catalysis and Mössbauer Parameter Calculations. For the [OH,His^+,--]Ni^{2+} and [H,His^+,--]Ni^{2+} (or [†H,His^+,--]Ni^{2+}) models, which we thought could correspond to C_{red1} and C_{red2}, respectively (ref 25 and this work), the QM part of QM/MM optimized structures was extracted, and smaller QM models were built by adding hydrogens to the Cβ atoms. Finally, we extracted the same atoms from the published PDB file and built hydrogen atoms for [OH-320] with Ni^{2+}, and [OH-600] with Ni^0, as possible X-ray models for the C_{red1} and C_{red2} states, respectively (Figure 1).[23]

In order to compare calculated Mössbauer quadrupole tensors and isomer shift parameters with available experimental data, we performed additional DFT calculations on these models, using the Slater-based ADF2009 code[50] with triple-ζ basis sets for all atoms, with the Vosko, Wilk, and Nusair (VWN) LDA functional[51,52] and the Becke−Perdew exchange-correlation potential.[53,54] For the quadrupole tensor [**Q**], we relied on an in-house program coupled to ADF output files, based on an analytical expression already published elsewhere.[55,56] From the three eigenvalues of [**Q**], we get $\Delta E_Q = (Q_{ii})_{max}(1 + \eta^2/3)$, where η is the asymmetry parameter defined as $\eta = |((Q_{ii})_{int} - (Q_{ii})_{min})/(Q_{ii})_{max}|$. In order to estimate the isomer shifts $\{\delta_{Fe}\}$, we computed electron densities $\{\rho_{Fe}\}$ at the Fe nucleus. The isomer shift values are derived from linear correlations between experimental isomer shifts of chemically related systems and corresponding electron densities. Selected data for ferrous and ferric-containing monomeric compounds are given in the Supporting Information. For delocalized mixed-valence Fe ions, we averaged the two previous ferrous and ferric correlations. Moreover, in order to determine whether the formal [Ni^{2+}-H^-] fragment in models [H,His^+,--]Ni^{2+} and [†H,His^+,--]Ni^{2+} was either Ni^{2+}-H^-, Ni^+-H, or Ni^0-H^+, or if the $[Fe_uFe_3S_4]^{+1}$ moiety was also affected by the addition of two electrons to the system via a hydride, charge population analyses were done on the basis of (1) the Mulliken partitioning scheme, which relies on equal sharing of the overlap charge population between two atoms, and (2) the Voronoi scheme, which integrates the charge density within appropriate atom-centered volumic cells.[57]

Results and Discussion

In the next four sections, we use crystallography and QM/MM methods to characterize the $COOH_x$-, OH_x-, and CN-bound structures, in order to get suitable models for the C_{red1} and the C_{red2} states. The fifth section deals with the calculation of Mössbauer parameters on these models and their comparison to experimental data.

(49) Nicolet, Y.; Amara, P.; Mouesca, J. M.; Fontecilla-Camps, J. C. *Proc. Natl. Acad. Sci. U.S.A.* **2009**, *106*(35), 14867–14871.

(50) te Velde, G.; Baerends, E. J. *J. Comput. Phys.* **1992**, *99*(1), 84–98.
(51) Painter, G. S. *J. Phys. Chem.* **1986**, *90*(22), 5530–5535.
(52) Vosko, S. H.; Wilk, L.; Nusair, M. *Can. J. Phys.* **1980**, *58*(8), 1200–1211.
(53) Becke, A. D. *Phys. Rev. A* **1988**, *38*(6), 3098–3100.
(54) Perdew, J. P.; Yue, W. *Phys. Rev. B* **1986**, *33*(12), 8800–8802.
(55) Horner, O.; Mouesca, J. M.; Solari, P. L.; Orio, M.; Oddou, J. L.; Bonville, P.; Jouve, H. M. *J. Biol. Inorg. Chem.* **2007**, *12*(4), 509–525.
(56) Zimmermann, R.; Ritter, G.; Spiering, H.; Nagy, D. L. *J. Phys. (Paris)* **1974**, *C6*, 439–442.
(57) Fonseca Guerra, C.; Handgraaf, J. W.; Baerends, E. J.; Bickelhaupt, F. M. *J. Comput. Chem.* **2004**, *25*, 189–210.

$COOH_x$ Form at −600 mV. The $COOH_x$-bound X-ray model (PDB 3B52) is the most homogeneous of the [COO-600], [OH-320], and [OH-600] *C. hydrogenoformans* C-cluster structures.[23] Our complete refined active site model is shown in Figure S1 (Supporting Information). Like in the original [COO-600] model, in the 65% occupied conformation of our revised [COO-600*rev*] model, the $Ni-C_{COO}$ bond completes the square planar coordination of this metal ion, and one of the $COOH_x$ oxygen atoms binds Fe_u, resulting in a distorted tetrahedral coordination. This oxygen also interacts with Lys563, whereas the other $COOH_x$ oxygen atom interacts with His93 (Figures 3 and S1). Further refinement led to a decrease of the $Ni-C_{COO}$ distance from 1.96 Å to 1.86 Å. In the vicinity of the active site (see also Supporting Information), we added alternative conformations: (1) for an Fe atom with a 20% occupancy in a position we call $^{\dagger}Fe_u$ that is very close to the major position of this unique iron ion in the [CN-320] X-ray model (see below) and (2) a 20% occupied conformation for the 260−267 segment and nearby residues 365 and 366 (†Seg), with His261 interacting with $^{\dagger}Fe_u$, each 20% occupied. Finally, a Ni-bound CO molecule located at the entrance/exit tunnel for gaseous substrates/products[18,22] and W_e (Figure 3), which interacts with a conserved water network, were added to the model with 35% occupancy. Interestingly, Ni-bound CO and W_e are potential substrates for CO_2 production.

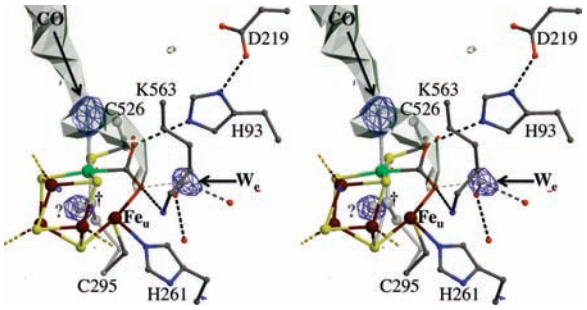

Figure 3. Stereo view of the [COO-600*rev*] model active site with the omit map contoured at 3.5 σ shown in blue and at −3.5 σ (red), where σ corresponds to the RMSD value of the map. Minor structural components are shown as gray balls and sticks. The ? represents a peak that may be explained by a putative Fe atom with 15% occupancy or that may be due to ripples originating from the cluster atoms. Putative CO and W_e molecules and the ? marked atom were left out of phase and structure factor calculations. † indicates the $^{\dagger}Fe_u$ position of the unique iron. A cavity calculation using a 0.8 Å probe radius and omitting the COO and CO ligands reveals a hydrophobic tunnel (shown in gray) that reaches the C-cluster. The three small red spheres represent conserved water molecules, whereas W_e is a water molecule only included in the [COO-600*rev*] and [OH-320]/[OH-320*rev*] models. Standard color codes are used for C, N, O, and S atoms, while the Ni and the Fe atoms are indicated in green and dark red, respectively, in Figures 3−6 and Figures S1 and S2 (Supporting Information).

QM/MM geometry optimizations for the COO^--bound and COOH-bound C-cluster (Table 1) indicate that most probably the [COO-600] structure corresponds to a Ni^{2+}-bound unprotonated carboxylate. COOH may be excluded because its optimized structure does not correspond to the revised model for the following reasons: (1) the Fe_u-O_1 and $N\zeta_{Lys563}-O_1$ distances are longer than observed and (2) there is a large difference between the $C-O_1$ and $C-O_2$ distances that might have been detected at 1.50 Å resolution. However, this does not exclude Ni-bound COOH as a catalytic intermediate. It is not clear from our calculations whether His93 is doubly protonated and interacts with both Asp219 and one oxygen atom from the bound carboxylate (Figure 3) or whether it is singly protonated and only interacts with the former. In [COO-600*rev*], the $N\varepsilon-O_2$ distance lies between the values calculated for the singly and doubly protonated states of His93 (Table 1).

OH_x Form at −320 mV. In our [OH-320*rev*] revised model, the main conformation corresponding to the bound OH_x is only 35% occupied, compared to 65% in the original [OH-320] model (Figure S2, Supporting Information). The remaining 30% of the electron density peak has been assigned to $COOH_x$ (Figure 4) like in the [COO-600] and [COO-600*rev*] models described above. Thus, in [OH-320*rev*], there is a mixture of more or less equivalent amounts of OH_x and $COOH_x$ (Figure 4). The 35%-occupied water molecule W_e in [COO-600*rev*] was modeled with a 65% occupancy in [OH-320*rev*] in order to match its temperature factor to those of atoms in its immediate vicinity. A 20% occupied alternative conformation of the 260−267 amino acid segment †Seg and nearby residues 365−366 was also added; this conformational change was also seen in [COO-600*rev*] and will be discussed below. In the 35%-occupied OH_x−bound [OH-320*rev*] model, Ni adopts a T-shaped coordination. Conversely, in the remaining 30%-occupied $COOH_x$−bound [OH-320*rev*] model, Ni has a regular square planar coordination like in [COO-600*rev*]. Fe_u displays a distorted tetrahedral coordination in both [COO-600*rev*] and [OH-320*rev*].

We were puzzled by the asymmetrical binding of OH_x in [OH-320] because we expected this ligand to bridge Fe_u and Ni^{2+} instead of being only bound to Fe_u. Previously, a sulfido species (most probably SH^-) was found to bridge

Table 1. QM/MM Optimized Ni^{2+}-Bound $COOH_x$ Models, Compared to [COO-600*rev*]

	models				
distances[a]	[COO-600*rev*] main conformation	[COO,His,--]Ni^{2+}	[COO,His^+,--]Ni^{2+}	[COOH,His,--]Ni^{2+}	[COOH,His^+,--]Ni^{2+}
$Ni-Fe_u$	2.8	2.84[b]	2.86	2.76	2.93
$Ni-S_u$	3.7	3.86	3.86	3.69	3.87
$Ni-C_{COO}$	1.9	1.87	1.86	1.84	1.85
$C-O_1$,[c] $C-O_2$	1.2, 1.2	1.34, 1.22	1.33, 1.24	1.41, 1.21	1.46, 1.21
$O_2(O_1)-N\varepsilon_{His93}$	3.0	3.22	2.68	(2.75)	2.81
Fe_u-O_1	2.0	2.02	2.04	2.45	2.22
$O_1-N\zeta_{Lys563}$	2.7	2.66	2.75	2.96	2.99
$Fe_u-N\varepsilon_{His261}$	2.1	2.35	2.33	2.30	2.34

[a] In Ångstroms. [b] Calculated distances are given with two significant figures after the period, although the precision of the calculations is expected to be ±0.05 Å [c] O_1 is the oxygen atom of COO that is bound to Fe_u.

these ions with Ni−S and Fe_u−S distances of 2.47 Å and 2.09 Å, respectively.[19] In [OH-320], the respective distances are 2.80 Å and 1.89 Å. It is not possible to discriminate between O^{2-}, OH^-, or H_2O on the basis of the electron density, so we tested the three possibilities with two protonation states for His93 and a Ni^{2+} oxidation state, as suggested by the poised −320 mV redox potential. Results of QM/MM geometry optimizations with a hydroxide ligand are shown in Table 2. In all [Ni^{2+}, OH^-] models, the hydroxide *bridges* Ni and Fe_u. Although the results shown in Table S2 (Supporting Information) also indicate a bridging binding mode for O^{2-}, this is a less likely ligand because it implies excessive negative charge at the active site. H_2O does not bridge the metal ions and is closer to Fe_u than to Ni (Table S3, Supporting Information). However, due to its interaction with either protonated or unprotonated His93, H_2O is further away from Fe_u and Lys563 than the corresponding peak in the omit map (Figure 4). In conclusion, we did not manage to reproduce the [OH-320*rev*] C-cluster geometry with Ni^{2+}.

In a recent *in vacuo* quantum study of a C-cluster model active site, Xie and Cao[58] also found a bridging mode when using a hydroxide ligand and a Ni ion in the +2 oxidation state. Like us, in calculations using a H_2O ligand, these authors found it to bind asymmetrically to both metals and concluded that this model represents the C_{red1} state, according to its assignment to [OH-320] by Jeoung and Dobbek (intermediate **I** in Figure 1). However, as mentioned above, our own H_2O models, generated including the protein matrix and allowing the whole system to move during optimization, do not fit the electron density in [OH-320].

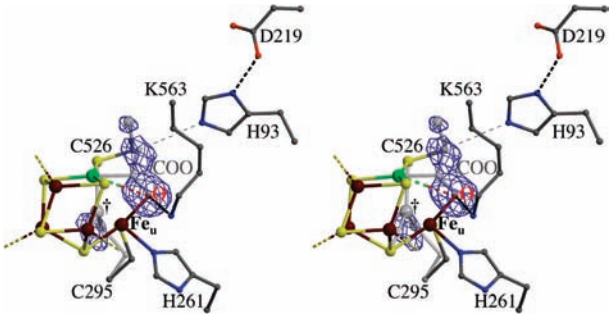

Figure 4. Stereo view of the [OH-320*rev*] model active site with the omit map contoured at 3.5 σ shown in blue. Alternative side chain conformations of Cys295 and Cys526, as well as COO and O (in red), were left out of phase and structure factor calculations. † indicates the $^{\dagger}Fe_u$ position of the unique iron. Minor structural components are shown as gray balls and sticks.

One argument to assign the [OH-320] model to C_{red1}[23] is the strong ENDOR signal from an exchangeable proton observed for this state,[11] which is compatible with a C-cluster OH_x ligand. Some of us have previously proposed that the OH^- ligand bridges Ni^{2+} and Fe_u in C_{red1},[25,59] a hypothesis that has been supported by the calculations discussed above. We excluded models containing the *extra* water molecule W_e, assuming that it is a product and most probably not part of an intermediate state of the reaction. In addition, we favored doubly protonated His93 because the C-cluster active site is already quite negatively charged. We thus retained [OH-320] with Ni^{2+} and [OH,His^+,--]Ni^{2+} as possible candidates for Mössbauer parameter calculations on the catalytically relevant C_{red1} state.

OH_x Form at −600 mV. When we superimposed [OH-320] and [OH-600], the root-mean square deviation was only 0.12 Å. In addition, our revised refinements of the [OH-600] model (PDB code 3B51) revealed that $COOH_x$ was present, like in the case of [OH-320] (see section above), but this time with 35% occupancy compared to 30% for OH_x. This result led us to stop further refinements on this model, which is, in fact, a mixture of [COO-600] and [OH-320], and used the [OH-320*rev*] model for subsequent calculations. The OH^- and H_2O ligands (Tables 3 and S4, Supporting Information) were subsequently geometry-optimized with the nickel ion in the Ni^0 state because the redox potential poised for [OH-600] should lead to a more reduced species than [OH-320]. Interestingly, in our calculations, we found that OH^- binds Fe_u and interacts only weakly with Ni (Table 3), as in [OH-320] and [OH-600]. Again, the optimized H_2O ligand lies further away from Fe_u and Lys563 than in the X-ray model, probably due to its interaction with His93 (Table S4). These results, along with their very similar structures, strongly suggest that [OH-320] and [OH-600] correspond to the same reduced redox state with Fe-bound OH^-. The asymmetric binding of this ligand in both [OH-320] and [OH-600] could be explained if the C-cluster in the starting C_{red1} fraction were reduced by two X-ray-induced photoelectrons.[60,61] C_{red1} reduction should result in OH^- dissociation. However, at $T = 100$ K, the X-ray data collection temperature, atomic movements are severely limited, and the ligand only moves away from Ni, without leaving the C-cluster. This new conformation is stable because the OH^- ligand occupies the position of one of the $COOH_x$ oxygen atoms.

Jeoung and Dobbek proposed that the [OH-600] form corresponds to the C_{red2} state (intermediate **IV** in Figure 1) with nickel in the formal Ni^0 redox state because

Table 2. QM/MM Optimized Active Site Models with Ni^{2+} and Bound OH^-, Compared to [OH-320*rev*]

	models				
distances[a]	[OH-320*rev*] main conformation	[OH,His,W_e]Ni^{2+} [b]	[OH,His^+,W_e]Ni^{2+}	[OH,His,--]Ni^{2+}	[OH, His^+,--]Ni^{2+}
Ni−Fe_u	2.8	2.69	2.72	2.71	2.72
Ni−S_u	3.5	3.64	3.58	3.43	3.64
Ni−O	2.8	1.97	1.98	2.11	1.97
Fe_u−O	1.9	2.06	2.07	2.01	2.07
O−$N\varepsilon_{His93}$	4.2	3.99	4.52	3.29	4.13
O−$N\zeta_{Lys563}$	2.5	2.75	2.79	2.67	2.78
Fe_u−N_{His261}	2.1	2.25	2.29	2.23	2.25

[a] In Ångstroms. [b] The conserved water network, though perturbed, is still present.

Table 3. QM/MM Optimized Active Site Models with Ni^0 and Fe_u-Bound OH^-, Compared to [OH-320*rev*]

	models				
distances[a]	[OH-320*rev*] main conformation	[OH,His,W_e]Ni^{0b}	[OH,His^+,W_e]Ni^0	[OH,His,--]Ni^0	[OH,His^+,--]Ni^0
$Ni-Fe_u$	2.8	2.77	2.87	2.71	2.87
$Ni-S_u$	3.5	3.78	3.84	3.77	3.80
Ni−O	2.8	3.06	3.04	3.03	3.09
Fe_u−O	1.9	2.12	2.05	2.13	2.26
$O-N\varepsilon_{His93}$	4.2	4.02	4.13	3.66	3.36
$O-N\zeta_{Lys563}$	2.5	2.65	2.52	2.66	2.70
Fe_u-N_{His261}	2.1	2.36	2.35	2.36	2.37

[a] In Ångstroms. [b] The conserved water network is still present though perturbed.

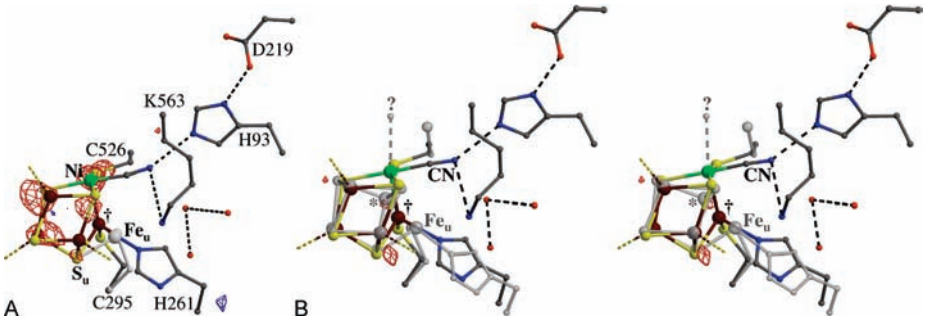

Figure 5. (A) Active site of [CN-320] original model (PDB code 3I39). (B) Stereo image of [CN-320*rev*] model. † indicates the $^{\dagger}Fe_u$ position of the unique iron. Residual [$F_{obs} - F_{calc}$] electron density maps are contoured at 3.5 σ (blue) and −3.5 σ (red). Minor structural components are shown as gray balls and sticks. The gray ∗ indicates a putative alternative position for Ni, completing a partially occupied [$NiFe_3S_4$] cluster (see text). An unidentified apical ligand to the Ni was also observed and is indicated by a ?.

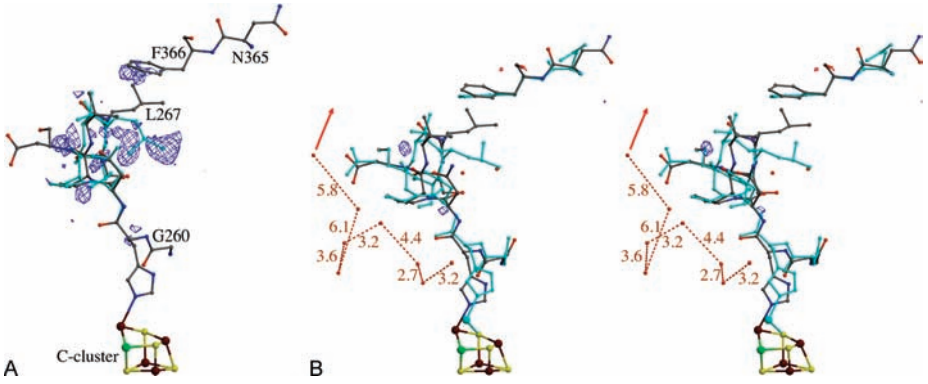

Figure 6. (A) The 260−267 amino acid segment (†Seg) and residues 365−366 in [CN-320] (PDB code 3I39). (B) Stereo view of [CN-320*rev*]. The alternative conformation (Seg) is shown in cyan. Distances between water molecules running roughly parallel to the segment are given in Ångstroms, and the red arrow indicates the protein surface. Residual [$F_{obs} - F_{calc}$] electron density maps are contoured at 3.5 σ (blue) and −3.5 σ (red). The three water molecules closest to the C-cluster are also shown in Figure 5.

C_{red2} has been postulated to be two-electron more-reduced than C_{red1}.[7,8] However, this model is problematic because of the loss in C_{red2} of the strong ENDOR signal observed for the C_{red1} state, which was attributed to the departure of OH^-.[11] In addition, the spin analysis of our QM/MM optimized models with Ni^0 and an OH^- bound to Fe_u (Table 3) shows that one of the electrons from Ni^0 is transferred to the [$Fe_uFe_3S_4$] cluster, reducing it to all-ferrous with 0 total charge and generating a Ni(I) species. This is against experimental evidence from UV−visible[10] and Mössbauer[9] studies, indicating that the electronic structure of the [$Fe_uFe_3S_4$] cluster does not change upon reduction and from EPR data,[12,17] suggesting that it remains in the +1 oxidation state with a total spin $S = 1/2$ in C_{red1} and C_{red2}. Besides, **g**-tensor components for Ni(I) are above 2.0,[62] while the C_{red2} state g_{av} is 1.86,[8] similar to that of a standard $[Fe_4S_4]^{+1}$ cluster. The same objection applies to the model of a C_{red2} state with a $Ni^{"0"}$ and a Fe_u-bound water proposed by Xie and Cao.[58] In addition, like for OH^-, a Fe_u-bound water molecule should be detectable by ENDOR spectroscopy.[11] The C_{red2} state was also proposed to consist of a Ni in the 0 oxidation state with no exogenous ligand,[17,32] but

(58) Xie, H. J.; Cao, Z. X. *Chin. J. Struct. Chem.* **2009**, *28*(11), 1525–1532.
(59) Volbeda, A.; Fontecilla-Camps, J. C. *Top. Organomet. Chem.* **2006**, *17*, 57–82.
(60) Liu, B.; Chen, Y.; Doukov, T.; Soltis, S. M.; Stout, C. D.; Fee, J. A. *Biochemistry* **2009**, *48*, 820–826.
(61) Garman, E. F. *Acta Crystallogr.* **2010**, *D66*, 339–351.
(62) Pietrzyk, P.; Podolska, K.; Sojka, Z. *J. Phys. Chem. A* **2008**, *112*, 12208–12219.

geometry optimization of this state ([--,His^+,--]Ni^0) also leads to a one-electron transfer from Ni to the [$Fe_uFe_3S_4$] cluster and a highly distorted [$NiFe_3S_4$] cluster (distances between 2.2 and 2.6 Å). This alternative Ni"0" model may therefore also be excluded as a possible structure for C_{red2}.

A different model for C_{red2}, with a bridging hydride between Fe_u and Ni^{2+}, was postulated by some of us.[25] In order to test this hypothesis, we geometry-optimized a model with a hydride initially placed at 2.88 Å from Ni and 2.08 Å from Fe_u (model [H,His^+,--]Ni^{2+}, see Materials and Methods). After the optimization, H^- moved to distances of 1.50 Å and 2.26 Å from Ni and Fe_u, respectively, whereas Ni adopted a distorted square planar coordination and Fe_u conserved a distorted tetrahedral coordination. Although the above results are clearly against the [OH-600] model with a Ni^0, we retained [OH-600] and [H,His^+,--]Ni^{2+} as potential candidates for the C_{red2} state in Mössbauer parameter calculations, for comparison purpose (see below).

C-Cluster Inhibition by Cyanide. In the recent 1.36-Å-resolution crystallographic study of a CN^- *Ch*CODH complex, Jeoung and Dobbek found that CN^- binding completes a square pyramidal coordination for Ni (including a Ni−Fe_u bond), while the unique iron has tetrahedral coordination.[33] This structure differs significantly from the recently reported 2.15-Å-resolution X-ray model of a CN-*Mt*CODH,[34] which proposed a bent axial Ni-bound cyanide ligand with this metal ion adopting a distorted tetrahedral coordination and with a OH_x ligand bound to Fe_u. This model is very similar to the one proposed for a 2.0-Å-resolution *Mb*CODH model[28] with a bent CO or formyl ligand. Examination of the corresponding electron density maps did not provide us with conclusive evidence favoring the modeled orientation of the putative CN^- or CO/formyl ligands (not shown). Consequently, only the 1.36 Å resolution *Ch*CODH CN^--bound structure,[33] where the cyanide is clearly hydrogen bonded to His93, was used in our calculations. Key distances at the [CN-320] active site are very similar in our revised [CN-320*rev*] model (Figure 5A and B, respectively) with the main conformation having 60% occupancy. As noted by Jeoung and Dobbek, the major position of the unique iron in [CN-320] corresponds to the minor $^{\dagger}Fe_u$ position found in [COO-600] and [COO-600*rev*] and in [OH-320] and [OH-320*rev*]. The addition of the major conformation of the 260−267 amino acid segment in [COO-600] and [OH-320] (Seg) with 40% occupancy explained the residual electron density in [CN-320] (Figure 6A). Moreover, we used the main alternative conformation of the 260−267 amino acid segment (†Seg, 60% occupancy) as a minor conformation in [COO-600*rev*] and [OH-320*rev*], as it fitted the unexplained density in [COO-600] and [OH-320] (Figure 6). These results suggest that the †Seg conformation and the $^{\dagger}Fe_u$ position in [CN-320] can result from effects other than CN^- binding.[33] As in the original model, the electron density is further explained by a 20% Fe_u occupancy, which corresponds to the major position of the unique iron in [COO-600*rev*] and [OH-320*rev*]. Furthermore, an additional ([Fe_4S_4] or [$NiFe_3S_4$]) cluster was added with 20% occupancy (Figure 5B). The latter resembles the [$NiFe_3S_4$] cluster in the previously reported *Rr*CODH structure.[20]

Table 4. Comparison between the QM/MM Optimized Model with CN^- Bound to Ni^{2+} and [CN-320*rev*]

	models	
distances[a]	[CN-320*rev*] main conformation	[†CN,His^+,--]Ni^{2+}
Ni−$^{\dagger}Fe_u$	2.6	2.74
Ni−S_u	3.9	3.90
C−N	1.2	1.17
Ni−C_{CN^-}	1.8	1.82
N_{CN^-}−$N\varepsilon_{His93}$	2.7	2.84
$^{\dagger}Fe_u$−C_{CN^-}	3.4	3.06
$^{\dagger}Fe_u$−$N\varepsilon_{His261}$	2.3	2.28

[a] In Ångstroms.

Table 6. Charge Analyses in Possible Models for C_{red1} and C_{red2}

atoms	Mulliken	Voronoi
	[OH,His^+,--]Ni^{2+}	
Ni	+0.06	+0.15
OH^-	−0.50	−0.48
	[H,His^+,--]Ni^{2+}	
Ni	−0.03	+0.43
H^-	−0.32	−0.87
	[†H,His^+,--]Ni^{2+}	
Ni	−0.04	+0.47
H^-	−0.31	−0.80

Table 5. Calculated Mössbauer Parameters Compared to the Experimental Values Available for C_{red1}

atoms[a]	Mössbauer parameters	exptl[b] C_{red1}	[OH-320]Ni^{2+}	[OH,His^+,--]Ni^{2+}	[OH-600]Ni^0	[H,His^+,--]Ni^{2+}	[†H,His^+,--]Ni^{2+}
FCII	$\delta(Fe_u)$	0.82	0.61	0.90	0.63	0.87	0.88
	η	−0.2	0.23	0.32	0.37	0.58	0.40
	ΔE_Q	2.82	2.40	2.60	1.90	2.04	2.37
FCIII	$\delta(Fe_2)$	0.62	0.47	0.73	0.41	0.75	0.73
	η	−0.6	0.38	0.44	0.53	0.14	0.69
	ΔE_Q	2.35	0.49	2.10	−1.23	2.27	2.23
$Fe^{II}Fe^{III}$	$\delta(Fe_3)$	0.53	0.38	0.54	0.41	0.55	0.52
	η	0.8	0.42	0.49	0.31	0.56	0.42
	ΔE_Q	1.12	1.07	1.60	1.15	1.61	1.60
$Fe^{II}Fe^{III}$	$\delta(Fe_4)$	0.53	0.41	0.42	0.44	0.44	0.41
	η	0.8	0.65	0.43	0.42	0.43	0.39
	ΔE_Q	1.12	0.99	1.15	0.88	1.13	1.06

[a] FCII, FCIII, and $Fe^{II}Fe^{III}$ correspond to Fe_u, Fe_2, and Fe_3Fe_4, respectively, in Figure 2. [b] Experimental data on C_{red1} state from ref 9; δ and ΔE_Q are in mm/s.

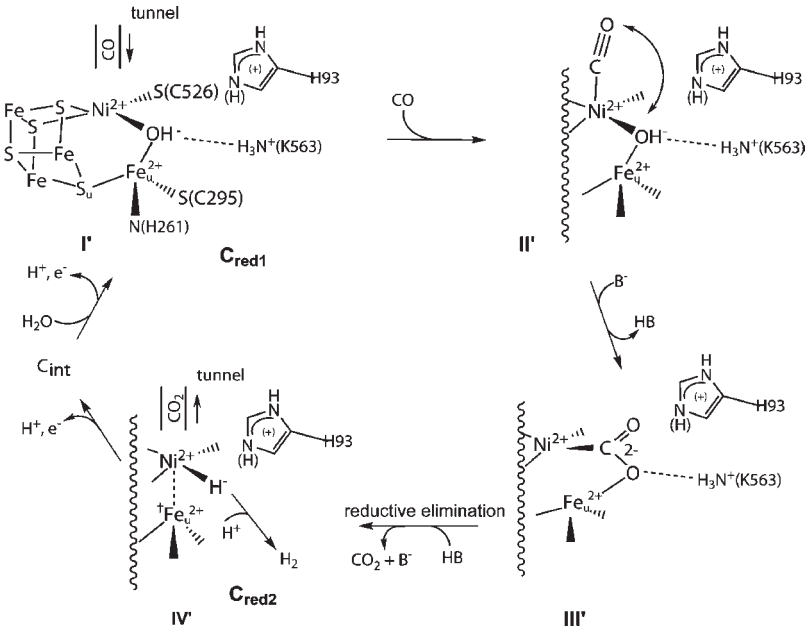

Figure 7. CO oxidation mechanism at the C-cluster. Although we cannot deduce it from our calculations, His93 could play the role of the base (B^-).

QM/MM geometry optimization of a model with Ni^{2+} and CN^- led to a structure that is very similar to [CN-320*rev*] (Table 4). One reason why CN^- does not bind C_{red2}[7,8] may be that it cannot displace the Ni-bound hydride; thus in addition to the [H,His^+,--]Ni^{2+} model, where the H^- was optimized in the major [OH-320] conformation, the hydride was also optimized starting from the CN^- carbon position in [CN-320]. After the calculations, the hydride is still bound to the Ni atom whose coordination is now undistorted square pyramidal. In this model, $^{\dagger}Fe_u$ is bound to Ni. We also tested the Ni"0" hypothesis with no ligand in this conformation ([†--,His^+,--]Ni^0) but, as in [--,His^+,--]Ni^0, Ni^0 was oxidized by one electron. Thus, in addition to [OH-600] and [H,His^+,--]Ni^{2+}, we retained [†H,His^+,--]Ni^{2+} as a candidate for the C_{red2} state.

Mössbauer Parameter Calculations and Orbital Analyses on Quantum Models. A spectroscopic study of *Rr*CODH and *Mt*CODH determined the Mössbauer parameters of the C_{red1} state and suggested that the corresponding values for the C_{red2} state are very similar.[9] We have constructed small QM models of the catalytically relevant species for which we wanted to calculate the Mössbauer parameters (see Materials and Methods), namely, [OH-320] with Ni^{2+} and [OH, His^+,--]Ni^{2+} for the C_{red1} state and [OH-600] with Ni^0, [H, His^+,--]Ni^{2+}, and [†H, His^+,--]Ni^{2+} for the C_{red2} state.

Our results (Tables 5 and S5, Supporting Information) clearly show that the [OH, His^+,--]Ni^{2+} structure where OH^- bridges Fe_u and Ni (Table 2) fits the experimental Mössbauer parameters for C_{red1}, whereas the [OH-320] structure with a terminally Fe-bound OH^- and Ni^{2+} does not. In particular, the experimental quadrupole splitting difference between FCII and FCIII (2.82 mm/s versus 2.35 mm/s, respectively) is nicely reproduced computationally (2.60 mm/s versus 2.10 mm/s, respectively). Moreover, although we compute a slight difference between the two other splittings (1.60 mm/s versus 1.15 mm/s), it should be mentioned that the experimental fitting procedure in ref 9 most probably constrained them to be equal

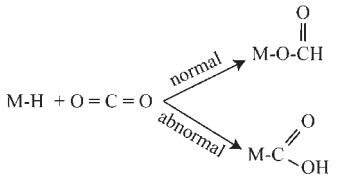

Figure 8. Possible CO_2 insertion into a metal hydride bond leading to either a formate (normal) or a carboxylate (abnormal) metal-bound species.

in order to reduce the number of free parameters; this was based on the assumption that the [$Fe_uFe_3S_4$] cluster geometry was cubane-like, which is clearly not the case. The agreement between theory and experimental results is therefore satisfying. The same holds true when one compares the measured 0.82, 0.62, 0.53, and 0.53 and computed 0.90, 0.73, 0.54, and 0.42 sets of isomer shifts (mm/s). Mössbauer parameters calculated for the [OH-600] model are very different from the ones reported for the C_{red1} state, while both [H,His^+,--]Ni^{2+} and [†H,His^+,--]Ni^{2+} hydride models are significantly closer. In particular, the values computed for [†H,His^+,--]Ni^{2+} are better because, experimentally, the Mössbauer data for C_{red2} are known to be relatively similar to those measured for C_{red1}.[9] However, from these data alone, the [H,His^+,--]Ni^{2+} model cannot be ruled out.

A role for a hydride as the electron reservoir in C_{red2}[25] could, in principle, be questioned. Indeed, experimentally, Ni most probably remains low spin at the +2 oxidation state,[9,13,15] whereas it cannot be excluded that, in our models, the formal $Ni^{2+}-H^-$ is actually Ni^0-H^+ or Ni^+-H. Analysis of the three models that fit Mössbauer data, namely, [OH,His^+,--]Ni^{2+}, [H,His^+,--]Ni^{2+}, and [†H,His^+,--]Ni^{2+}, shows similar charge distributions and magnetic properties (Table 5). More precisely, Mulliken and Voronoi charges have been computed for [OH, His^+,--]Ni^{2+} and the putative C_{red2} models (Table 6). A similar charge distribution for all of the models favors a $Ni^{2+}-H^-$ species for the possible C_{red2} states [H,His^+,--]Ni^{2+} and [†H,His^+,--]Ni^{2+}, which is supported by X-ray

absorption studies.[15] In addition, the absence of a ^{61}Ni ENDOR signal in C_{red1} and C_{red2}[11] helps in discriminating between our [H,His$^+$,--]Ni^{2+} and [†H,His$^+$,--]Ni^{2+} models. Indeed, in [H,His$^+$,--]Ni^{2+}, the hydride interacts with the paramagnetic Fe_u at 2.26 Å and thus could be expected to exhibit an ENDOR signal which is not observed in C_{red2}.[11] By contrast, in [†H,His$^+$,--]Ni^{2+}, the H$^-$−†Fe$_u$ distance is 3.16 Å, and consequently, no ENDOR signal should be expected because the Ni is diamagnetic. [†H,His$^+$,--]Ni^{2+} is therefore our preferred candidate for C_{red2}. This reasoning is based on the hypothesis that the hyperfine coupling constant observed by ENDOR spectroscopy for the exchangeable OH$^-$ proton in the C_{red1} state originates from Fe_u. This is also supported by the absence of a ^{61}Ni ENDOR signal. For reasons explained elsewhere, we could not test this hypothesis by computing reliable hyperfine coupling constants (see the Supporting Information).

Conclusions

Heterogeneity of C-Cluster in CODH Crystals. The spectroscopic and structural studies on Ni-containing CODH of the past two decades have provided multiple insights into the complex enzymatic mechanism of this enzyme. Here, we have used the recent high resolution structures of *Ch*CODH, where $COOH_x$ and OH_x bind at the C-cluster active site,[23] to further investigate the catalytic mechanism of reversible anaerobic CO oxidation. In addition, a subsequent high-resolution structure of CN$^-$-bound *Ch*CODH[33] has yielded valuable information concerning conformational changes near the C-cluster. An analysis of these structures and our revised refinements confirmed the heterogeneity of the samples and revealed features that provided further insights into the mechanism:

(1) In [COO-600], we found structural evidence (Figures 3 and S1B, Supporting Information) for partially occupied CO and H_2O (W_e) that are substrates/products of the reaction producing CO_2 or reducing it to CO. CO reaches the C-cluster through a hydrophobic tunnel and binds apically to Ni (intermediate **II′** in Figure 7), whereas W_e interacts with a conserved water network near the equatorial plane of the Ni coordination sphere.

(2) The main conformation of the 260−267 amino acid segment in [CN-320] (†Seg) is a minor component of the [COO-600*rev*] and [OH-320*rev*] structures, whereas the main conformation for this segment (Seg) in the latter is a minor component in [CN-320*rev*] (Figure 6). Two major positions for the unique iron, Fe_u and †Fe$_u$, are associated with Seg and †Seg, respectively, and we find that this conformational change is not uniquely caused by CN$^-$ binding. A network of water molecules runs parallel to this segment (Figure 6), which suggests that the observed conformational change of the 260−267 amino acid segment may be instrumental in the transfer of water, a substrate of the CO oxidation and a product of CO_2 reduction, between the C-cluster active site and the protein surface. The extra water W_e found in [OH-320], [OH-320*rev*], and to a lesser extent [COO-600*rev*] may represent the closest bucket to the active site in a firefighters' bucket brigade scheme for water diffusion. Hydrophilic cavity calculations for these two structures (not shown) indicate that additional protein dynamics would be required for the proposed diffusion pathway to exist. Interestingly, analysis of the corresponding region in the *Mt*CODH structure shows that it has higher temperature factors than its immediate environment.[63]

Revised Catalytic Cycle. The revised crystallographic refinements, QM/MM geometry optimizations, and Mössbauer parameter calculations described above lead to the catalytic mechanism presented in Figure 7, which is an updated version of the one previously proposed by some of us.[25]

In the CO oxidation direction, CO reaches the active site via the hydrophobic tunnel apical to the Ni square planar coordination consisting of three S atoms and the Ni−Fe_u bridging OH$^-$ (intermediate **I′** in Figure 7). Mössbauer parameters calculated for the corresponding QM structure fit the experimental values attributed to the C_{red1} state. Once CO is bound (intermediate **II′**), it reacts with OH$^-$ to form COO, formally charged −2 (intermediate **III′**). Reductive elimination of CO_2 leads to the structure corresponding to the C_{red2} state. Our results suggest that this state consists of a hydride bound to the Ni ion that adopts a square pyramidal coordination. The unique iron goes from the Fe_u to the †Fe$_u$ position adopting a regular tetrahedral coordination that includes a Ni−Fe bond, correlated with the 260−267 amino acid segment conformational change, which needs to be at least as fast as enzyme turnover in order to be operational during catalysis.[64] The mechanism in the CO_2 reduction direction requires the unusual insertion of CO_2 to a metal-hydride to form a metallocarboxylate (**IV′** to **III′** in Figures 7 and 8). This was only indirectly observed once in a cobalt complex.[35] CO_2 insertion into a metal hydride bond usually forms a formate bound to the metal through a M−O bond (the "normal" mode).[37] However, at the C-cluster, the protein matrix prevents the arrival of CO_2 in the orientation leading to the transition state of the metal formate formation. Indeed, we could not manually dock a transition state with the substrate C atom facing the hydride[65] due to steric hindrance by His93 and Lys563 side chains, whereas the reverse orientation of CO_2 (i.e., C toward Ni and O toward H$^-$) is favored by the hydrophobic tunnel (Figure 3). In addition, hydrogen bonding from His93 and Lys563 side chains favors a carboxylate (intermediate **III′** in Figure 7) over a formate. Finally, the binding to iron induces the weakening and subsequent cleavage of the carboxylate single C−O bond that generates CO and H_2O (**III′** to **II′** in Figure 7), as illustrated by a Pd mimetic model compound.[66]

(63) Volbeda, A.; Fontecilla-Camps, J. C. *J. Biol. Inorg. Chem.* **2004**, *9*(5), 525–532.
(64) Henzler-Wildman, K. A.; Lei, M.; Thai, V.; Kerns, S. J.; Karplus, M.; Kern, D. *Nature* **2007**, *450*, 913–916.
(65) Ohnishi, Y. Y.; Matsunaga, T.; Nakao, Y.; Sato, H.; Sakaki, S. *J. Am. Chem. Soc.* **2005**, *127*, 4021–4032.

In summary, we favor the hydride as the putative redox active ligand of the Ni atom in the C_{red2} state for the following reasons:

(1) It occupies the position of CN^-, which is known not to bind C_{red2}.[7,8]

(2) CODHs have weak hydrogenase activity,[67] producing H_2 as a side reaction (possibly from intermediate **IV′** of Figure 7) of the catalytic cycle.

(3) The proposition of hydroxide binding to Fe_u with a Ni^0 for the C_{red2} state[23] (Figure 1) does not explain the loss of the strong ENDOR signal from a solvent-exchangeable proton, when going from C_{red1} to C_{red2}.[11] In addition, our calculations show that a Ni^0 species with or without a ligand cannot keep the two electrons, as one of them migrates to the $[Fe_uFe_3S_4]$ cluster. This, in turn, is against experimental evidence from EPR,[12] UV−visible,[10] and Mössbauer spectroscopy.[9,17] A Ni-bound hydride not only satisfies the experimental data discussed above but it also fits our calculations showing that the two electrons stay with the hydrogen atom. Consequently, the cluster remains $[Fe_uFe_3S_4]^{+1}$, and the Ni^{2+} remains low-spin, as indicated by experiments.[13,15] In conclusion, H^- acts as a strongly localized electron reservoir for CO_2 reduction and CO oxidation.

(4) No ^{61}Ni ENDOR signal was observed in either C_{red1} or C_{red2}, indicating that the ENDOR signal for the exchangeable proton in C_{red1} arises from Fe_u. This observation, combined with the fact that in our preferred model the $^{\dagger}H^-$ is terminally bound to Ni (i.e., not bound to $^{\dagger}Fe_u$), explains the absence of an ENDOR signal for the hydride in C_{red2}. Finally, to close the CO oxidation cycle, the C_{red2} to C_{red1} step requires the elimination of two protons and two electrons via an intermediate species (C_{int} in Figure 7). By analogy with the Ni−C state of [NiFe]-hydrogenase,[68] some of us proposed a $Ni^{3+}Fe_u$ bridging hydride for the C_{int} state.[59] A water molecule reaching the active site at either the C_{red2} or the C_{int} state and electron transfer to the B-cluster would then lead to the C_{red1} state.

In conclusion, the cycle depicted in Figure 7 fits spectroscopic and structural experimental evidence concerning CODHs' catalytic mechanism. Further investigations on the protein dynamics, which could add information on the substrate/product routes to and from the active site, are underway.

Acknowledgment. We appreciate the help from the staff of the computing facility provided by the Commissariat à l'Energie Atomique (CEA/DSV/GIPSI), Saclay, France, and thank the CEA and CNRS for institutional funding. We also thank Dr. Daniel L. Dubois and Prof. Kenneth G. Caulton for helpful discussions.

Supporting Information Available: Crystallographic refinements, refinement statistics, active site of [COO-600] original model and stereo image of [COO-600*rev*] model, active site of [OH-320] original model and stereo image of [OH-320*rev*] model, QM/MM calculations, QM/MM optimized Ni^{2+} active site models, QM/MM optimized Ni^0 active site models, Mössbauer parameter calculations, complete Mössbauer data, ENDOR parameter calculations, heterogeneity of C cluster in CODH crystals, and occupancies at the C-cluster active site. This material is available free of charge via the Internet at http://pubs.acs.org.

(66) Dubois, M. R.; Dubois, D. L. *Acc. Chem. Res.* **2009**, *42*(12), 1974–1982.
(67) Menon, S.; Ragsdale, S. W. *Biochemistry* **1996**, *35*(49), 15814–15821.
(68) Fontecilla-Camps, J. C.; Volbeda, A.; Cavazza, C.; Nicolet, Y. *Chem. Rev.* **2007**, *107*(10), 4273–4303.